

# Highly Durable $\text{Na}_2\text{V}_6\text{O}_{16}\cdot 1.63\text{H}_2\text{O}$ Nanowire Cathode for Aqueous Zinc-Ion Battery

Ping Hu,<sup>†</sup> Ting Zhu,<sup>†</sup> Xuanpeng Wang,<sup>†</sup> Xiujian Wei,<sup>†</sup> Mengyu Yan,<sup>‡</sup> Jiantao Li,<sup>†</sup> Wen Luo,<sup>†</sup> Wei Yang,<sup>†</sup> Wencui Zhang,<sup>†</sup> Liang Zhou,<sup>\*,†</sup> Zhiqiang Zhou,<sup>†</sup> and Liqiang Mai<sup>\*,†</sup>

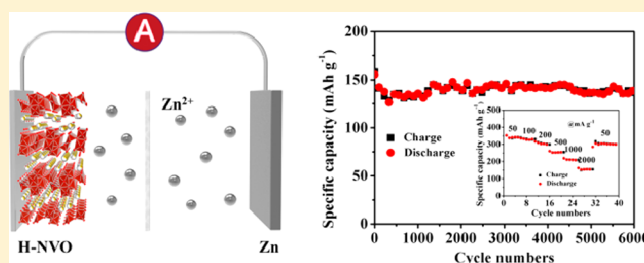
<sup>†</sup>State Key Laboratory of Advanced Technology for Materials Synthesis and Processing, International School of Materials Science and Engineering, Wuhan University of Technology, Wuhan 430070, China

<sup>‡</sup>Materials Science and Engineering Department, University of Washington, Seattle, Washington 98195, United States

## S Supporting Information

**ABSTRACT:** Rechargeable aqueous zinc-ion batteries are highly desirable for grid-scale applications due to their low cost and high safety; however, the poor cycling stability hinders their widespread application. Herein, a highly durable zinc-ion battery system with a  $\text{Na}_2\text{V}_6\text{O}_{16}\cdot 1.63\text{H}_2\text{O}$  nanowire cathode and an aqueous  $\text{Zn}(\text{CF}_3\text{SO}_3)_2$  electrolyte has been developed. The  $\text{Na}_2\text{V}_6\text{O}_{16}\cdot 1.63\text{H}_2\text{O}$  nanowires deliver a high specific capacity of  $352 \text{ mAh g}^{-1}$  at  $50 \text{ mA g}^{-1}$  and exhibit a capacity retention of 90% over 6000 cycles at  $5000 \text{ mA g}^{-1}$ , which represents the best cycling performance compared with all previous reports. In contrast, the  $\text{NaV}_3\text{O}_8$  nanowires maintain only 17% of the initial capacity after 4000 cycles at  $5000 \text{ mA g}^{-1}$ . A single-nanowire-based zinc-ion battery is assembled, which reveals the intrinsic  $\text{Zn}^{2+}$  storage mechanism at nanoscale. The remarkable electrochemical performance especially the long-term cycling stability makes  $\text{Na}_2\text{V}_6\text{O}_{16}\cdot 1.63\text{H}_2\text{O}$  a promising cathode for a low-cost and safe aqueous zinc-ion battery.

**KEYWORDS:** Aqueous zinc-ion battery,  $\text{Na}_2\text{V}_6\text{O}_{16}\cdot 1.63\text{H}_2\text{O}$ , nanowire, single-nanowire battery, zinc ion intercalation and deintercalation



Aqueous batteries have captured significant scientific and technical interest due to their high safety and low cost.<sup>1–15</sup> Among aqueous batteries, zinc-ion batteries (ZIBs) are especially attractive due to the high gravimetric capacity of Zn ( $820 \text{ mAh g}^{-1}$ ) and high redox potential of  $\text{Zn}^{2+}/\text{Zn}$  ( $-0.78 \text{ V}$  versus standard hydrogen electrode). To date, manganese-based oxides,<sup>16–20</sup> Prussian blue analogs,<sup>21–23</sup> and vanadium-based materials<sup>24–32</sup> have been studied as cathodes for ZIBs. Manganese oxides, including  $\alpha$ -,  $\beta$ -,  $\gamma$ -, and  $\delta$ - $\text{MnO}_2$  with different tunnel structures have been extensively investigated as intercalation hosts for  $\text{Zn}^{2+}$ .<sup>18,33–35</sup> However,  $\text{MnO}_2$  suffers from fast capacity fading in aqueous electrolyte. By introducing a  $\text{MnSO}_4$  additive in the electrolyte to suppress the dissolution of  $\text{Mn}^{2+}$  during cycling, Liu et al. realized a ZIB with enhanced energy density and cycling stability.<sup>16</sup> Prussian blue analogs represent another attractive family of ZIB cathode materials. However, the low capacity ( $\sim 50 \text{ mAh g}^{-1}$ ) and  $\text{O}_2$  evolution at high voltage ( $\sim 1.7 \text{ V}$  versus  $\text{Zn}^{2+}/\text{Zn}$ ) hinder their further application.<sup>21–23</sup>

The merits of vanadium-based ZIB cathode materials include their abundant resources, low cost, and good safety.<sup>36–46</sup> Nazar et al. constructed a zinc ion and crystalline water stabilized vanadium oxide bronze ( $\text{Zn}_{0.25}\text{V}_2\text{O}_5\cdot n\text{H}_2\text{O}$ ), and the assembled  $\text{Zn}/\text{Zn}_{0.25}\text{V}_2\text{O}_5\cdot n\text{H}_2\text{O}$  battery delivered an energy density of  $450 \text{ Wh L}^{-1}$  and a capacity retention of  $\sim 80\%$  after 1000 cycles.<sup>24</sup> Kim et al. presented a layered  $\text{LiV}_3\text{O}_8$  intercalation

cathode with a high specific capacity of  $172 \text{ mAh g}^{-1}$ , and 75% of the maximum capacity could be retained after 65 cycles at  $133 \text{ mA g}^{-1}$ .<sup>26</sup> Huang et al. developed a NASICON-structured  $\text{Na}_3\text{V}_2(\text{PO}_4)_3$  ZIB cathode, which delivered a capacity of  $97 \text{ mAh g}^{-1}$  at  $0.5 \text{ C}$  and retained 74% capacity after 100 cycles.<sup>27</sup> In general, the cycling performance of vanadium-based ZIB cathodes is unsatisfactory.

Single-nanowire electrochemical devices are an effective tool for the in situ exploration of the intrinsic electrochemical processes at the nanoscale.<sup>47–53</sup> Mai et al. first reported a single-nanowire electrochemical device, enabling in situ detection of the intrinsic reason for electrode capacity fading in Li-ion-based batteries.<sup>45</sup> Such devices were then utilized to monitor the structure and conductivity evolution in sodium-ion batteries.<sup>46</sup> The single-nanowire ZIB device can be designed and assembled to detect the intrinsic electrochemical reaction mechanisms in aqueous ZIBs. However, to the best of our knowledge, there is no report on single-nanowire-based ZIBs.

Herein, we designed a novel ZIB cathode material,  $\text{Na}_2\text{V}_6\text{O}_{16}\cdot 1.63\text{H}_2\text{O}$  (H-NVO) nanowire with facile electrochemical  $\text{Zn}^{2+}$  intercalation and highly reversible characteristics.

**Received:** November 18, 2017

**Revised:** January 22, 2018

**Published:** February 3, 2018

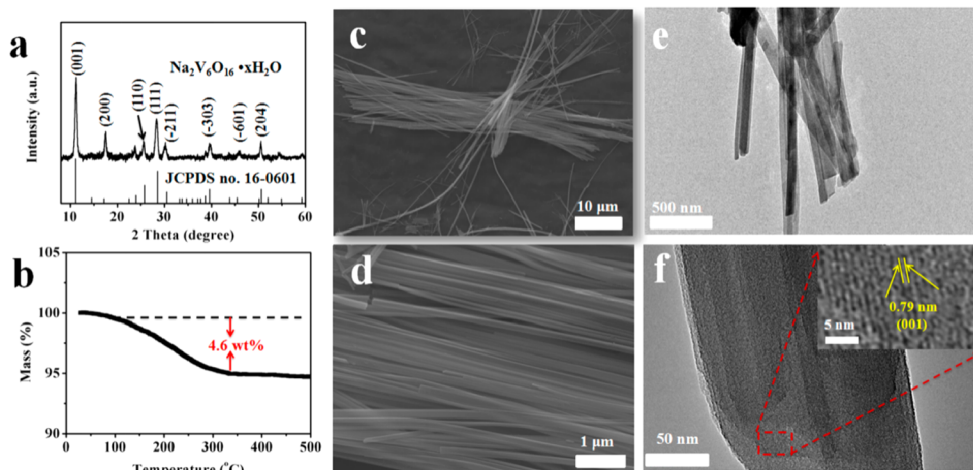


**Figure 1.** (a) XRD pattern, (b) TGA curve, (c, d) SEM images, and (e, f) TEM images of H-NVO nanowires.

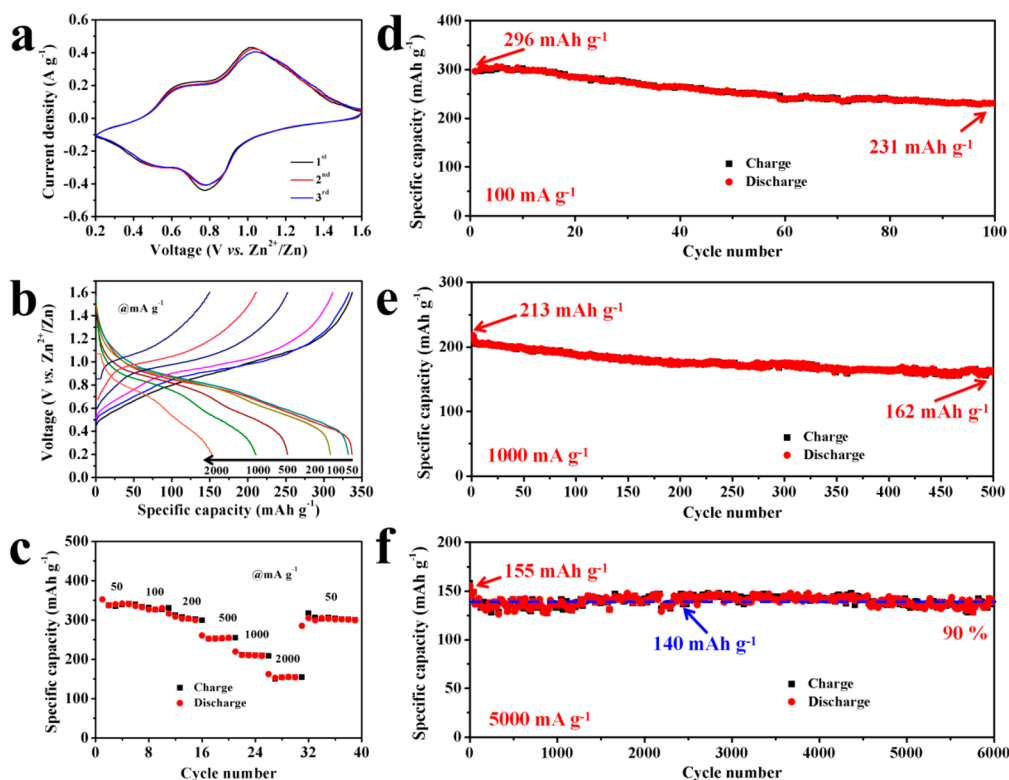


**Figure 2.** (a) Cyclic voltammograms of H-NVO at a scan rate of  $0.2 \text{ mV s}^{-1}$  with the electrochemical window of 0.2–1.6 V versus  $\text{Zn}^{2+}/\text{Zn}$ . (b) Charge–discharge curves of the H-NVO at various current densities ranging from 50 to  $2000 \text{ mA g}^{-1}$ . (c) Rate performance of the H-NVO at various current densities. Cycling performances of the H-NVO at (d) 100, (e) 1000, and (f)  $5000 \text{ mA g}^{-1}$ .

The  $\text{Na}_2\text{V}_6\text{O}_{16}\cdot 1.63\text{H}_2\text{O}$  nanowires deliver a high specific capacity of  $352 \text{ mAh g}^{-1}$  at  $50 \text{ mA g}^{-1}$  and ultralong cycle life (90% capacity retention after 6000 cycles at  $5000 \text{ mA g}^{-1}$ ) within the potential window of 0.2–1.6 V versus  $\text{Zn}^{2+}/\text{Zn}$ . On the basis of electrochemical characterizations, ex situ X-ray diffraction (XRD), ex situ X-ray photoelectron spectroscopy (XPS), and single-nanowire zinc-ion battery results, we disclosed that the existence of structural water would contribute a great improvement to the cycling stability of ZIBs.

The H-NVO nanowires were synthesized by a simple hydrothermal method.<sup>43</sup> The XRD pattern of the sample (Figure 1a) can be indexed well to the pure monoclinic phase  $\text{Na}_2\text{V}_6\text{O}_{16}\cdot x\text{H}_2\text{O}$  with the space group of P21/m (JCPDS no.

16-0601), and the sample displays a high crystalline degree. The weight percentage of crystalline water can be determined by the weight loss in the temperature range of 100–350 °C from the thermogravimetric analysis (TGA) curve. Based on a weight loss of 4.6 wt % (Figure 1b), the  $x$  value in  $\text{Na}_2\text{V}_6\text{O}_{16}\cdot x\text{H}_2\text{O}$  is determined to be 1.63. Scanning electron microscopy (SEM) results show that the H-NVO is composed of nanowires with lengths of 10–40  $\mu\text{m}$  and widths of 40–200 nm (Figure 1c,d). The primary nanowires have a tendency to form bundles. Transmission electron microscopy (TEM) images (Figure 1e,f) confirm that the H-NVO nanowires have relatively uniform diameters. The interplanar spacing (0.79 nm) matches well with the (001) lattice fringe (Figure 1f inset).

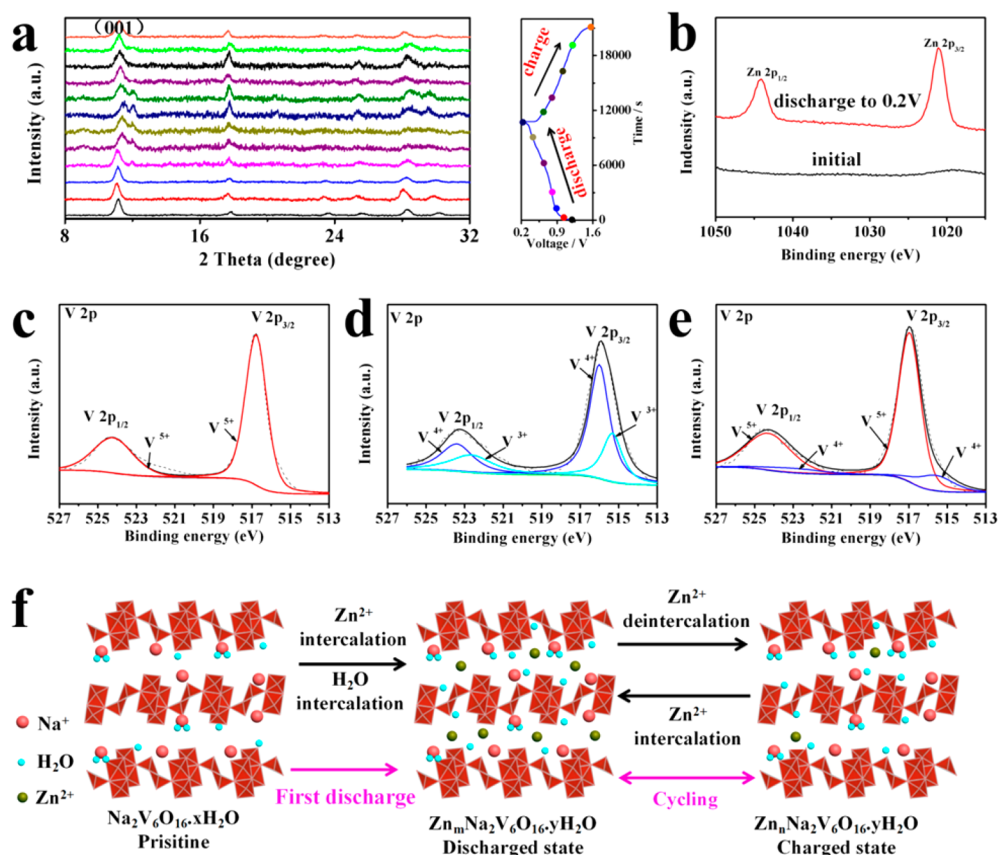


**Figure 3.** Ex situ XRD patterns and XPS spectra of H-NVO collected at different electrochemical states in  $\text{Zn}(\text{CF}_3\text{SO}_3)_2$  electrolyte at  $100 \text{ mA g}^{-1}$ : (a) ex situ XRD patterns; (b) high-resolution Zn 2p spectra; high-resolution V 2p spectrum at (c) initial state, (d) discharged to 0.2 V, and (e) charged to 1.6 V. (f) Schematic illustrations of water intercalation accompanying  $\text{Zn}^{2+}$  intercalation into H-NVO at the first discharge process and  $\text{Zn}^{2+}$  deintercalation and intercalation upon electrochemical charge and discharge processes. Here,  $x < y$  and  $m > n$ .

The H-NVO nanowires can be converted into  $\text{NaV}_3\text{O}_8$  (NVO) nanowires by annealing in air at  $400^\circ\text{C}$ . The obtained NVO nanowires have diameters of 60–500 nm and lengths of several micrometers (Figure S1a–c). Under high-resolution TEM measurement, the (002) lattice spacing (0.68 nm) of NVO can be clearly observed (Figure S1d,e). No mass loss between 100 and  $350^\circ\text{C}$  can be observed in the TGA curve of NVO, confirming that the crystalline water has been completely removed during annealing in the air (Figure S1f). The textural properties of the products are characterized by nitrogen sorption. The H-NVO and NVO nanowires show specific surface areas of 19.7 and  $9.5 \text{ m}^2 \text{ g}^{-1}$ , respectively (Figure S2).

Figure 2 shows the electrochemical performances of the assembled Zn/H-NVO batteries. The CV curves between 0.2 and 1.6 V versus  $\text{Zn}^{2+}/\text{Zn}$  at a scan rate of  $0.2 \text{ mV s}^{-1}$  are displayed in Figure 2a. There are two pairs of redox peaks located at 1.03/0.78 and 0.64/0.46 V, which are caused by the zinc ion deintercalation and intercalation during the charge and discharge processes. For NVO, four reduction peaks (0.46, 0.69, 0.87, and 1.20 V) and three oxidation peaks (0.57, 0.91, and 1.32 V) can be observed in the second CV curve at  $0.1 \text{ mV s}^{-1}$ , which is quite different from that of H-NVO (Figure S3).

The charge and discharge curves of H-NVO under various current densities are shown in Figure 2b, from which obvious charge and discharge plateaus can be discerned. In the rate performance study, the H-NVO exhibits average discharge capacities of 352, 335, 316, 261, 219, and  $162 \text{ mA g}^{-1}$  at current densities of 50, 100, 200, 500, 1000, and  $2000 \text{ mA g}^{-1}$  (Figure

2c), respectively. After the cycling at high current densities, the current density is reduced to  $50 \text{ mA g}^{-1}$ , and an average discharge capacity of  $304 \text{ mA h g}^{-1}$  can be recovered, corresponding to  $\sim 90\%$  of the initial capacity. This implies that the synthesized H-NVO possesses considerable rate capability. When tested at  $100 \text{ mA g}^{-1}$ , the H-NVO delivers a high initial discharge capacity of  $296 \text{ mA h g}^{-1}$ , maintaining as high as  $231 \text{ mA h g}^{-1}$  after 100 cycles (Figures 2d and S4). Meanwhile, the H-NVO exhibits a high Coulombic efficiency, stabilizing in the range of 98.6–100.6% (Figure S5). At a current density of  $1000 \text{ mA g}^{-1}$ , 75% of the initial capacity can be retained after 500 cycles (Figure 2e). Remarkably, when measured at  $5000 \text{ mA g}^{-1}$ , the H-NVO exhibits a discharge capacity of  $158 \text{ mA h g}^{-1}$ ; 90% of the initial discharge capacity is retained after 6000 cycles (Figures 2f and S6). Compared to H-NVO, the NVO exhibits inferior electrochemical performances in terms of specific capacity, rate capacity, and cycling stability (Figure S7), indicating that the structural water plays a significant role in improving the electrochemical performances of H-NVO. At a current density of  $5000 \text{ mA g}^{-1}$ , the discharge capacity decreases from 120 to  $20 \text{ mA h g}^{-1}$  after 4000 cycles, corresponding to a capacity retention of 17% (Figure S7d). In addition, the morphology of the H-NVO nanowires can be well maintained after cycling (Figure S8). The electrochemical performances of recently reported vanadium-based ZIB cathode materials are summarized in Table S1. Compared with the recently reported vanadium-based cathodes, the H-NVO

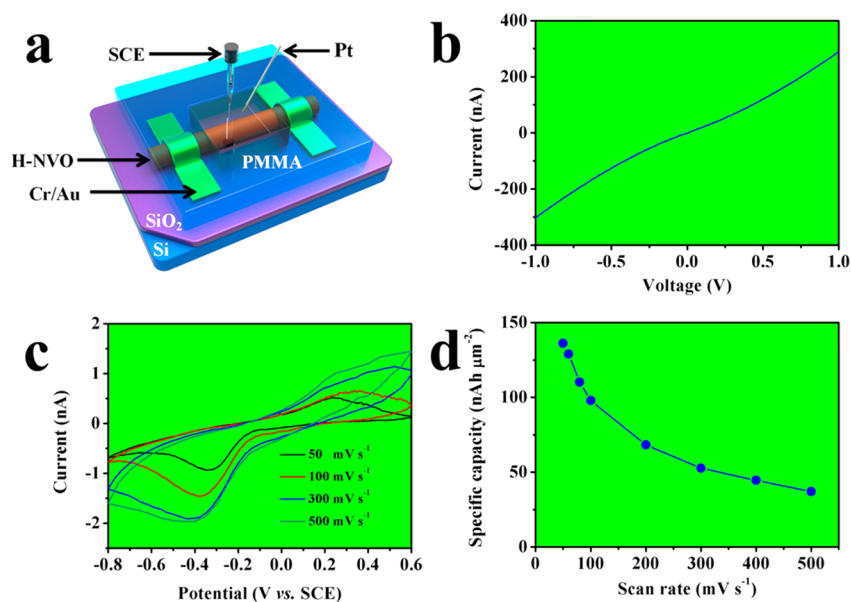


**Figure 4.** Electrochemical performances of the as-prepared H-NVO single-nanowire ZIB. (a) Schematic illustration of the single-nanowire ZIB. (b) The single-nanowire transport property. (c) The CV curves tested at scan rates from 50 to 500  $\text{mV s}^{-1}$ . (d) The specific capacitances versus different scan rates.

demonstrates the best electrochemical performance in terms of specific capacity and cycling stability.

To better understand the underlying reasons for the excellent cyclability and good rate performance of HVO, CV curves at various sweep rates ( $0.1\text{--}0.8 \text{ mV s}^{-1}$ ) were measured (Figure S9a), and detailed kinetics analysis was performed. The power-law relationship between current ( $i$ ) and scan rate ( $\nu$ ) is given by:<sup>40</sup>

$$i = a\nu^b \quad (1)$$

where  $a$  and  $b$  are adjustable parameters. The  $b$  value may reflect the rate-limiting step in the electrochemical process and thus the charge-storage mechanism. A  $b$  value of 0.5 indicates a diffusion-controlled process, while a  $b$  value of 1.0 suggests a surface-controlled process. By plotting  $\log(i)$  as a function of  $\log(\nu)$ , the  $b$  value can be determined from the slope of the plots. The  $b$  values for peak 1 and peak 2 are determined to be 0.63 and 0.66, respectively (Figure S9b). The calculated  $b$  values imply that the solid-state zinc-ion diffusion is the rate-limiting step for charge storage.

The Nyquist plots are shown in Figure S10a. The zinc-ion diffusion coefficient could be calculated from the low-frequency plots according to the following equation:

$$D = \frac{R^2 T^2}{2A^2 n^4 F^4 C^2 \sigma^2} \quad (2)$$

where  $R$  is the gas constant,  $T$  is the absolute temperature,  $A$  is the electrode area,  $n$  is the number of electrons per formula during oxidation,  $F$  is the Faraday constant,  $C$  is the concentration of zinc ions, and  $\sigma$  is the Warburg factor. The Warburg factor,  $\sigma$ , can be derived from the following equation:<sup>53–55</sup>

$$Z' = R_D + R_L + \sigma\omega^{-1/2} \quad (3)$$

The fitted lines (Figure S10b) indicate  $\sigma$  values of 56.7 and  $36.8 \text{ cm}^2 \text{ s}^{-1/2}$  for H-NVO and NVO, respectively. Thus, the zinc-ion diffusion coefficient of H-NVO and NVO could be calculated to be ca.  $1.24 \times 10^{-13}$  and  $2.95 \times 10^{-13} \text{ cm}^2 \text{ s}^{-1}$ ,

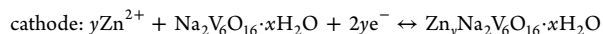
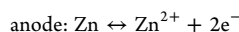
respectively. These values are comparable to the sodium-ion diffusion coefficients in  $\text{Na}_2\text{V}_6\text{O}_{16} \cdot 1.63\text{H}_2\text{O}$  and  $\text{NaV}_3\text{O}_8$  in an organic electrolyte (normally at the magnitude of  $\sim 10^{-13} \text{ cm}^2 \text{ s}^{-1}$ ).<sup>43,56</sup>

The ex situ XRD was carried out to validate the structural stability of H-NVO during the charge and discharge processes (Figure 3a). Upon slight discharge ( $\text{Zn}^{2+}$  intercalation) to 1.0 V, the (001) reflection shifts to lower  $2\theta$  positions (from  $11.19^\circ$  to  $11.10^\circ$ ). According to a recent report, this left shift in  $2\theta$  position is caused by the intercalation of  $\text{H}_2\text{O}$  into the  $(\text{V}_3\text{O}_8)^-$  interlayers, which would occur accompanying the  $\text{Zn}^{2+}$  intercalation.<sup>25</sup> Upon deep discharge to 0.2 V, the (001) reflection shifts to higher  $2\theta$  positions (from  $11.10^\circ$  to  $11.39^\circ$ ), corresponding to the decrease of cell parameter  $c$  from 0.797 to 0.783 nm. The decrease in the cell parameter  $c$  can be ascribed to the strong electrostatic interaction between the intercalated  $\text{Zn}^{2+}$  and the  $(\text{V}_3\text{O}_8)^-$  layers.<sup>27</sup> During the subsequent charge process, the  $\text{Zn}^{2+}$  deintercalation leads to the shift of (001) reflection to lower  $2\theta$  positions (from  $11.39^\circ$  to  $11.21^\circ$ ). Besides the peak shift in position, a new diffraction peak appears at  $11.99^\circ$  when discharged to 0.8 V, and its intensity increases with discharge processing. An inverse trend can be observed during subsequent charge. After full charging, the XRD pattern of the electrode is quite similar to that of the pristine electrode before electrochemical reaction, suggesting that the  $\text{Zn}^{2+}$  intercalation and deintercalation in H-NVO is highly reversible.

To explore the surface composition and valence states of V during  $\text{Zn}^{2+}$  insertion and extraction, ex situ XPS spectra of the H-NVO at different charge and discharge stages were collected. The Zn 2p core level spectra of H-NVO in the original and discharged (0.2 V) states are shown in Figure 3b. No signals for zinc can be detected in the XPS spectrum of original H-NVO. When discharged to 0.2 V, an obvious Zn  $2p_{3/2}$ – $2p_{1/2}$  spin-orbit doublet can be observed, indicating the successful intercalation of  $\text{Zn}^{2+}$  into H-NVO. The original H-NVO shows a V  $2p_{3/2}$ – $2p_{1/2}$  spin-orbit doublet for V(V), in which the V  $2p_{3/2}$  peak is located at 516.8 eV, and the V  $2p_{1/2}$  peak is

located at 524.1 eV (Figure 3c).<sup>57,58</sup> When discharged to 0.2 V, the V(V) is reduced to V(IV) and V(III) with V 2p<sub>3/2</sub>/V 2p<sub>1/2</sub> binding energy values of 516/523.3 and 515.3/522.6 eV (Figure 3d), respectively. After recharging to 1.6 V, most of the V(IV) and V(III) are reoxidized to V(V) accompanying the extraction of Zn<sup>2+</sup> (Figure 3e). The XPS results confirm the reversible intercalation/deintercalation of Zn<sup>2+</sup> in H-NVO during discharge and charge.

Based on the above results, the overall electrochemical reaction of the Zn/H-NVO battery can be described as follows:



The schematic illustration of Zn<sup>2+</sup> intercalation into and deintercalation from the H-NVO during the discharge and charge processes is shown in Figure 3f. During the first discharge process, the Zn<sup>2+</sup> intercalation is accompanied by the insertion of water molecules into the interlayers. Upon subsequent charge and discharge processes, the Zn<sup>2+</sup> is reversibly deintercalated from and intercalated into H-NVO.

Single-nanowire ZIB using an H-NVO single nanowire as the working electrode, platinum (Pt) wire as the counter electrode, saturated calomel electrode (SCE) as the reference electrode, and aqueous Zn(CF<sub>3</sub>SO<sub>3</sub>)<sub>2</sub> solution as the electrolyte was fabricated to investigate the intrinsic electrochemical processes of aqueous ZIB (Figure 4a). Figure S11a shows the structure of a single-nanowire ZIB testing system under SEM; the device is covered by poly(methyl methacrylate), while only the part contains 4 μm in length (150 nm in width) of the nanowire (Figure S11b) is exposed as the working electrode. The transport property of the single nanowire is determined by testing the current–voltage (*I*–*V*) curve (Figure 4b). The conductivity of the H-NVO reaches a high value of 67 S m<sup>-1</sup>, indicating that the H-NVO nanowire exhibits an excellent electrical conductivity. The CV responses at scan rates from 50 to 500 mV s<sup>-1</sup> within the potential range of -0.8 – 0.6 V are shown in Figure 4c. Broad redox pairs appear in the CV curves of the single-nanowire device, which are caused by the Zn<sup>2+</sup> deintercalated from/intercalated into H-NVO at nanoscale. The area specific capacity of the nanowire can be calculated from the CV results (Figure 4d). The H-NVO exhibits high surface capacities of 136, 129, 110, 98, 68, 52, 45, and 37 nAh μm<sup>-2</sup> at the scan rates of 50, 60, 80, 100, 200, 300, 400, and 500 mV s<sup>-1</sup>, respectively (Figure 4d). Based on the electrochemical tests of single-nanowire ZIB, it can be concluded that the H-NVO nanowire exhibits high electrical conductivity and current-carrying capacity. The fabrication of single-nanowire ZIB would push the fundamental and practical research of nanowire electrode materials for energy storage applications.

In conclusion, a highly durable aqueous Zn/Na<sub>2</sub>V<sub>6</sub>O<sub>16</sub>·1.63H<sub>2</sub>O battery is developed. The H-NVO nanowire cathode delivers a high specific capacity of 352 mAh g<sup>-1</sup> at 50 mA g<sup>-1</sup>, long-term cycle stability (a capacity retention of 90% after 6000 cycles), and good rate performance. Based on ex situ XRD and XPS characterizations and the single-nanowire ZIB results, we confirm that the H-NVO can provide an ultrastable skeleton structure for highly reversible Zn<sup>2+</sup> intercalation and deintercalation. This study suggests that the H-NVO is a promising cathode material for highly durable, low-cost, and safe aqueous ZIBs. This study also highlights the significant role of structured water in enhancing the electrochemical perform-

ances, especially the cycling stability, of certain ZIB cathode materials.

## ■ ASSOCIATED CONTENT

### Supporting Information

The Supporting Information is available free of charge on the ACS Publications website at DOI: 10.1021/acs.nanolett.7b04889.

Additional details on synthesis, structure and electrochemical characterization, and nanowire fabrication. Figures showing structural characterization, adsorption–desorption isotherms, cyclic voltammograms, Coulombic efficiency, charge and discharge curves, electrochemical performances, SEM results, and CV curves. A table showing electrochemical performance. (PDF)

## ■ AUTHOR INFORMATION

### Corresponding Authors

\*E-mail: liangzhou@whut.edu.cn.

\*E-mail: mlq518@whut.edu.cn.

### ORCID

Liang Zhou: 0000-0001-6756-3578

Liqiang Mai: 0000-0003-4259-7725

### Author Contributions

L.Q.M., P.H., and T.Z. designed the experiments. P.H., T.Z., X.P.W., and X.J.W. performed the experiments. P.H., T.Z., L.Z., M.Y.Y., J.T.L., W.Y., W.C.Z., and Z.Q.Z. discussed the interpretation of results and co-wrote the paper.

### Notes

The authors declare no competing financial interest.

## ■ ACKNOWLEDGMENTS

This work was supported by the National Natural Science Fund for Distinguished Young Scholars (grant no. 51425204), the National Natural Science Foundation of China (grant nos. 51521001, 21673171, and 51502226), the National Key Research and Development Program of China (grant no. 2016YFA0202603), the Programme of Introducing Talents of Discipline to Universities (grant no. B17034), and the Fundamental Research Funds for the Central Universities (WUT: 2016III001, 2016III002, 2017III009, 2017III008, and 2016III012).

## ■ REFERENCES

- (1) Bai, Y.; Zhou, X.; Zhan, C.; Ma, L.; Yuan, Y. F.; Wu, C.; Chen, M. Z.; Chen, G. H.; Ni, Q.; Wu, F.; Shahbazian-Yassar, R.; Wu, T. P.; Lu, J.; Amine, K. *Nano Energy* **2017**, *32*, 10–18.
- (2) Zuo, W. H.; Zhu, W. H.; Zhao, D. F.; Sun, Y. F.; Li, Y. Y.; Liu, J. P.; Lou, X. W. *Energy Environ. Sci.* **2016**, *9*, 2881–2891.
- (3) Wang, F.; Lin, Y. M.; Suo, L. M.; Fan, X. L.; Gao, T.; Yang, C. Y.; Han, F. D.; Qi, Y.; Xu, K.; Wang, C. S. *Energy Environ. Sci.* **2016**, *9*, 3666–3673.
- (4) Shan, X. Q.; Charles, D. S.; Lei, Y. K.; Qiao, R. M.; Wang, G. F.; Yang, W. L.; Feyngenson, M.; Su, D.; Teng, X. W. *Nat. Commun.* **2016**, *7*, 13370.
- (5) Pasta, M.; Wessells, C. D.; Huggins, R. A.; Cui, Y. *Nat. Commun.* **2012**, *3*, 1149.
- (6) Wang, F.; Suo, L. M.; Liang, Y. J.; Yang, C. Y.; Han, F. D.; Gao, T.; Sun, W.; Wang, C. S. *Adv. Energy Mater.* **2017**, *7*, 1600922.
- (7) Wang, Y. G.; Yi, J.; Xia, Y. Y. *Adv. Energy Mater.* **2012**, *2*, 830–840.
- (8) Yamada, Y. K.; Usui, K. J.; Sodeyama, K.; Ko, S.; Tateyama, Y.; Yamada, A. *Nature Energy* **2016**, *1*, 16129.

- (9) Dong, X. L.; Chen, L.; Su, X. L.; Wang, Y. G.; Xia, Y. Y. *Angew. Chem., Int. Ed.* **2016**, *55*, 7474–7477.
- (10) Suo, L. M.; Borodin, O.; Gao, T.; Olguin, M.; Ho, J.; Fan, X. L.; Luo, C.; Wang, C. S.; Xu, K. *Science* **2015**, *350*, 938–943.
- (11) Luo, J. Y.; Cui, W. J.; He, P.; Xia, Y. Y. *Nat. Chem.* **2010**, *2*, 760–765.
- (12) Lee, J. H.; Ali, G. L.; Kim, D. H.; Chung, Y. K. *Adv. Energy Mater.* **2017**, *7*, 1601491.
- (13) Dong, X. L.; Chen, L.; Liu, J. Y.; Haller, S.; Wang, Y. G.; Xia, Y. Y. *Sci. Adv.* **2016**, *2*, e1501038.
- (14) Wessells, C. D.; Peddada, S. V.; Huggins, R. A.; Cui, Y. *Nano Lett.* **2011**, *11*, 5421–5425.
- (15) Li, B.; Nie, Z. M.; Vijayakumar, M.; Li, G. S.; Liu, J.; Sprengle, V.; Wang, W. *Nat. Commun.* **2015**, *6*, 6303.
- (16) Pan, H. L.; Shao, Y. Y.; Yan, P. F.; Cheng, Y. W.; Han, K. S.; Nie, Z. M.; Wang, C. M.; Yang, J. H.; Li, X. L.; Bhattacharya, P.; Mueller, K. T.; Liu, J. *Nature Energy* **2016**, *1*, 16039.
- (17) Xu, C. J.; Li, B. H.; Du, H. D.; Kang, F. Y. *Angew. Chem., Int. Ed.* **2012**, *51*, 933–935.
- (18) Alfaruqi, M. H.; Mathew, V.; Gim, J.; Kim, S. J.; Song, J. J.; Baboo, J. P.; Choi, S. H.; Kim, J. *Chem. Mater.* **2015**, *27*, 3609–3620.
- (19) Zhang, N.; Cheng, F. Y.; Liu, Y. C.; Zhao, Q.; Lei, K. X.; Chen, C. C.; Liu, X. S.; Chen, J. *J. Am. Chem. Soc.* **2016**, *138*, 12894–12901.
- (20) Zhang, B. H.; Liu, Y.; Wu, X. W.; Yang, Y. Q.; Chang, Z.; Wen, Z. B.; Wu, Y. P. *Chem. Commun.* **2014**, *50*, 1209–1211.
- (21) Liu, Z.; Pulletikurthi, G.; Endres, F. *ACS Appl. Mater. Interfaces* **2016**, *8*, 12158–12164.
- (22) Zhang, L. Y.; Chen, L.; Zhou, X. F.; Liu, Z. P. *Sci. Rep.* **2016**, *5*, 18263.
- (23) Hou, Z. G.; Zhang, X. Q.; Li, X. N.; Zhu, Y. C.; Liang, J. W.; Qian, Y. T. *J. Mater. Chem. A* **2017**, *5*, 730–738.
- (24) Zhang, L. Y.; Chen, L.; Zhou, X. F.; Liu, Z. P. *Adv. Energy Mater.* **2015**, *5*, 1400930.
- (25) Kundu, D. P.; Adams, B. D.; Duffort, V.; Vajargah, S. H.; Nazar, L. F. *Nature Energy* **2016**, *1*, 16119.
- (26) He, P.; Yan, M. Y.; Zhang, G. B.; Sun, R. M.; Chen, L. N.; An, Q. Y.; Mai, L. Q. *Adv. Energy Mater.* **2017**, *7*, 1601920.
- (27) Alfaruqi, M. H.; Mathew, V.; Song, J. J.; Kim, S. J.; Islam, S. F.; Pham, D. T.; Jo, J.; Kim, S.; Baboo, J. P.; Xiu, Z. L.; Lee, K. S.; Sun, Y. K.; Kim, J. *Chem. Mater.* **2017**, *29*, 1684–1984.
- (28) Li, G. L.; Yang, Z.; Jiang, Y.; Jin, C. H.; Huang, W.; Ding, X. L.; Huang, Y. H. *Nano Energy* **2016**, *25*, 211–217.
- (29) Li, G. L.; Yang, Z.; Jiang, Y.; Zhang, W. X.; Huang, Y. H. *J. Power Sources* **2016**, *308*, 52–57.
- (30) Senguttuvan, P.; Han, S. D.; Kim, S.; Lipson, A. L.; Tepavcevic, S.; Fister, T. T.; Bloom, I. D.; Burrell, A. K.; Johnson, C. S. *Adv. Energy Mater.* **2016**, *6*, 1600826.
- (31) Kaveevivitchai, W.; Manthiram, A. *J. Mater. Chem. A* **2016**, *4*, 18737–18741.
- (32) Jo, J. H.; Sun, Y. K.; Myung, S. T. *J. Mater. Chem. A* **2017**, *5*, 8367–8375.
- (33) Lee, B.; Lee, H. R.; Kim, H.; Chung, K. Y.; Cho, B. W.; Oh, S. H. *Chem. Commun.* **2015**, *51*, 9265–9268.
- (34) Alfaruqi, M. H.; Gim, J.; Kim, S. J.; Song, J. J.; Jo, J.; Kim, S.; Mathew, V.; Kim, J. *J. Power Sources* **2015**, *288*, 320–327.
- (35) Lee, J.; Ju, J. B.; Cho, W. I.; Oh, S. H.; Cho, B. W. *Electrochim. Acta* **2013**, *112*, 138–143.
- (36) Wang, X. P.; Niu, C. J.; Meng, J. S.; Hu, P.; Xu, X. M.; Wei, X. J.; Zhou, L.; Zhao, K. N.; Luo, W.; Yan, M. Y.; et al. *Adv. Energy Mater.* **2015**, *5*, 1500716.
- (37) Xia, C.; Guo, J.; Lei, Y. J.; Liang, H. F.; Zhao, C.; Alshareef, H. N. *Adv. Mater.* **2018**, *30*, 1705580.
- (38) Zhao, Y. Y.; Han, C. H.; Yang, J. W.; Su, J.; Xu, X. M.; Li, S.; Xu, L.; Fang, R. P.; Jiang, H.; Zou, X. D.; Song, B.; Mai, L. Q.; Zhang, Q. J. *Nano Lett.* **2015**, *15*, 2180–2185.
- (39) Armstrong, A. R.; Lyness, C.; Panchmatia, P. M.; Islam, M. S.; Bruce, P. G. *Nat. Mater.* **2011**, *10*, 223–229.
- (40) Yan, M. Y.; He, P.; Chen, Y.; Wang, S. Y.; Wei, Q. L.; Zhao, K. N.; Xu, X.; An, Q. Y.; Shuang, Y.; Shao, Y. Y.; Mueller, K. T.; Mai, L. Q.; Liu, J.; Yang, J. H. *Adv. Mater.* **2018**, *30*, 1703725.
- (41) Moretti, A.; Passerini, S. *Adv. Energy Mater.* **2016**, *6*, 1600868.
- (42) Yan, M. Y.; Zhao, L. Z.; Zhao, K. N.; Wei, Q. L.; An, Q. Y.; Zhang, G. B.; Wei, X. J.; Ren, W. H.; Mai, L. Q. *Adv. Funct. Mater.* **2016**, *26*, 6555–6562.
- (43) He, H. N.; Jin, G. H.; Wang, H. Y.; Huang, X. B.; Chen, Z. H.; Sun, D.; Tang, Y. G. *J. Mater. Chem. A* **2014**, *2*, 3563–3570.
- (44) Peng, L. L.; Zhu, Y.; Fang, Z. W.; Chu, W. S.; Wang, X.; Xie, Y. J.; Li, Y. F.; Cha, J. J.; Yu, G. H.; Peng, X. *Nano Lett.* **2017**, *17*, 6273–6279.
- (45) Zhu, Y.; Peng, L. L.; Chen, D. H.; Yu, G. H. *Nano Lett.* **2016**, *16*, 742–747.
- (46) Song, Y.; Liu, T. Y.; Yao, B.; Kou, T. Y.; Feng, D. Y.; Liu, X. X.; Li, Y. *Small* **2017**, *13*, 1700067.
- (47) Liu, Z.; Zhan, Y.; Shi, G.; Moldovan, S.; Gharbi, M.; Song, L.; Ma, L. L.; Gao, W.; Huang, J. Q.; Vajtai, R.; Banhart, F.; Sharma, P.; Lou, J.; Ajayan, P. M. *Nat. Commun.* **2012**, *3*, 879.
- (48) Mai, L. Q.; Dong, Y. J.; Xu, L.; Han, C. H. *Nano Lett.* **2010**, *10*, 4273–4278.
- (49) Xu, X.; Yan, M. Y.; Tian, X. C.; Yang, C. C.; Shi, M. Z.; Wei, Q. L.; Xu, X.; Mai, L. Q. *Nano Lett.* **2015**, *15*, 3879–3884.
- (50) Duan, X. J.; Gao, R. X.; Xie, P.; Cohen-Karni, Y.; Qing, Q.; Choe, H. S.; Tian, B. Z.; Jiang, X. C.; Lieber, C. M. *Nat. Nanotechnol.* **2012**, *7*, 174–179.
- (51) Huang, J. Y.; Zhong, L.; Wang, C. M.; Sullivan, J. P.; Xu, W.; Zhang, L. Q.; Mao, S. X.; Hudak, N. S.; Liu, X. H.; Subramanian, A.; et al. *Science* **2010**, *330*, 1515–1520.
- (52) Hu, P.; Yan, M. Y.; Wang, X. P.; Han, C. H.; He, L.; Wei, X. J.; Niu, C. J.; Zhao, K. N.; Tian, X. C.; Wei, Q. L.; Li, Z. J.; Mai, L. Q. *Nano Lett.* **2016**, *16*, 1523–1529.
- (53) Xu, L.; Jiang, Z.; Qing, Q.; Mai, L. Q.; Zhang, Q. J.; Lieber, C. M. *Nano Lett.* **2013**, *13*, 746–751.
- (54) Shi, Y.; Wang, J. Z.; Chou, S. L.; Wexler, D.; Li, H. J.; Ozawa, K.; Liu, H. K.; Wu, Y. P. *Nano Lett.* **2013**, *13*, 4715–4720.
- (55) Chou, S. L.; Wang, J. Z.; Liu, H. K.; Dou, S. X. *J. Phys. Chem. C* **2011**, *115*, 16220–16227.
- (56) Yao, B.; Zhang, J.; Kou, T. Y.; Song, Y.; Liu, T. Y.; Li, Y. *Adv. Sci.* **2017**, *4*, 1700107.
- (57) Chao, D. L.; Xia, X. H.; Liu, J. L.; Fan, Z. X.; Ng, C. F.; Lin, J. Y.; Zhang, H.; Shen, Z. X.; Fan, H. J. *Adv. Mater.* **2014**, *26*, 5794–5800.
- (58) Mendiola, J.; Casanova, R.; Barbaux, Y. *J. Electron Spectrosc. Relat. Phenom.* **1995**, *71*, 249–261.